Monthly Notices of the ROYAL ASTRONOMICAL SOCIETY

MNRAS **541,** 3696–3708 (2025) https://doi.org/10.1093/mnras/staf1209
Advance Access publication 2025 July 24

The RAWS Project – I. Do AGNs quench their activity in cosmic filaments at redshifts up to $z \sim 0.6$?

M. S. R. Hassan, Z. Z. Abidin ★ and A. A. Nazri

Centre for Astronomy & Astrophysics Research, Department of Physics, Faculty of Science, Universiti Malaya, 50603 Kuala Lumpur, Malaysia

Accepted 2025 July 18. Received 2025 July 2; in original form 2025 May 9

ABSTRACT

The role of cosmic filaments in galaxy evolution remains uncertain, with conflicting evidence for both enhancement and suppression of star formation (SF) and active galactic nucleus (AGN) activity. In this first paper of the RAWS (RACS-WISE-SCOS-SDSS) project, we investigate the radio properties of galaxies in filaments by analysing source counts of radio sources from the Rapid ASKAP Continuum Survey (RACS), cross-matched with data from the Wide-field Infrared Survey Explorer (WISE), SuperCOSMOS Sky Survey (SCOS), and Sloan Digital Sky Survey (SDSS) filament reconstructions. Two samples – RAWS-low and RAWS-mid – were derived from RACS-low (887.5 MHz) and RACS-mid (1367.5 MHz), respectively. Each sample was subdivided into (1) all RAWS galaxies, (2) RAWS filament galaxies, and (3) RAWS non-filament galaxies. We constructed normalized Euclidean 1.4-GHz source counts for all subsamples. The results show that AGNs dominate all samples. The source counts for subsamples (1) and (3) agree well with those from previous radio surveys. However, we observe a clear suppression in the source counts of filament galaxies (subsample 2) across both RACS frequencies. This suggests a lower surface density of AGN in filamentary environments compared to field galaxies, possibly due to environmental processes such as ram-pressure stripping, gas depletion, or intergalactic medium (IGM) interactions. These findings are consistent with simulations predicting gradual quenching in intermediate-density environments. While our results support the idea that filaments may suppress AGN activity up to $z \sim 0.6$, further investigation is needed to understand their dual role in both quenching and fuelling galaxy evolution.

Key words: methods: statistical – galaxies: active – galaxies: evolution – intergalactic medium – large-scale structure of Universe – radio continuum: galaxies.

1 INTRODUCTION

Superclusters, a structure of 100-Mpc scale, are the largest structure in the Universe, and they are a home for regions of different density enhancements (e.g. Abell 1958; Bahcall 1988; Tully et al. 2014; Chon, Böhringer & Zaroubi 2015), and they encompass a variety of environments, including cosmic filaments (10-Mpc scale), galaxy clusters (1-Mpc scale) and galaxy groups (0.1-Mpc scale), along with larger, less dense structures such as voids and sheets which also contribute to their composition. Some of these environments and their respective embedded constituents have been extensively studied for the past few decades. For example, galaxy clusters are found to be the densest regions in the Universe (Carlberg et al. 1997; Poggianti et al. 2010), and their constituents not only include galaxies of different morphologies (e.g. Dressler 1980; Pranger et al. 2013; Marasco et al. 2023), but also high fractions of intracluster medium (e.g. Jones & Forman 1990; Mohr, Mathiesen & Evrard 1999; Zhang et al. 2024b), dark matter (DM; e.g. Zwicky 1937; Kravtsov & Borgani 2012; Montes & Trujillo 2018) and magnetic field (e.g. Carilli & Taylor 2002; Govoni & Feretti 2004; Osinga et al. 2022). This diversity of environments within superclusters underscores their significance as a dynamic and complex framework for studying the interactions and evolution of galaxies, DM, and physical processes across various density scales.

However, investigation into astronomical entities in other environments, in particular cosmic filaments (hereafter, filaments), has only recently been explored, although the characteristics of filamentary structures had been observed using different observational and theoretical techniques many decades ago (e.g. Postman, Geller & Huchra 1988; Quintana et al. 1997; Gray et al. 2002; Pimbblet, Drinkwater & Hawkrigg 2004; Stoica et al. 2005). For instance, observationally, the detection of filaments has predominantly relied on mapping the spatial distribution of galaxies, as evidenced by large and extensive galaxy redshift surveys, such as the Centre for Astrophysics redshift survey (de Lapparent, Geller & Huchra 1986), the Sloan Digital Sky Survey (SDSS, York et al. 2000), the Six-degree-Field Galaxy Survey (Jones et al. 2004), the Two-degree-Field Galaxy Redshift Survey (Cole et al. 2005), the Galaxy and Mass Assembly survey (GAMA; Driver et al. 2011), the Two Micron All Sky Survey (Huchra et al. 2012) and the Visible Multi-Object Spectrograph (VIMOS) Public Extragalactic Redshift Survey (VIPERS, Scodeggio et al. 2018). The spatial distribution of galaxies probed by these galaxy redshift surveys reveal that galaxies in filaments are distributed

★ E-mail: zzaa@um.edu.my

along a thread-like structure connecting two or more galaxy clusters. These redshift surveys have also been used to examine the physical properties and characteristics of galaxies residing within filamentary structures (e.g. Porter et al. 2008; Bonjean et al. 2020; O'Kane et al. 2024).

Despite their significant structure in the cosmic web, filaments are less dense than that of galaxy clusters due to their lower galaxy number density and broader spatial extent (e.g. Galárraga-Espinosa et al. 2020). While galaxy clusters represent the densest environments in the Universe, filaments provide an intermediate-density environment that offers valuable insights into galaxy formation and evolution. Since properties of galaxies are known to be affected by their environments (e.g. Vollmer 2013; Coccato et al. 2019; Kinyumu et al. 2023), studying galaxies in filaments is equally important as galaxy clusters for understanding their evolutionary pathways and put constraints on the properties of filaments. Unlike galaxy clusters, filaments encompass a diverse range of environmental conditions, such as sites with the largest fraction of matter (e.g. Cautun et al. 2014), the existence of the warm-hot intergalactic medium (e.g. Zhang et al. 2024a) and the distribution of Mpc-scale of diffuse synchrotron emission (e.g. Govoni et al. 2019; Botteon et al. 2020). These environmental conditions can significantly shape the evolutionary pathways of their galaxies, leading to distinct differences from those observed in high-density cluster environments (e.g. Dressler 1980; Kodama et al. 2001). However, the study of galaxy evolution in filaments has gained attention only quite recently compared to extensive research on galaxy clusters.

Using data from the GAMA survey, Alpaslan et al. (2015) analysed galaxy properties such as colour, brightness, and morphology within large-scale structures, including filaments, building upon earlier work by Porter et al. (2008). Their findings indicate that filament galaxies are not exclusively red and exhibit colour bimodality, unlike cluster galaxies at low redshift, which are predominantly red. Even though filament galaxies are not predominantly red, they exhibit a decreasing trend in the specific star formation rate (sSFR) with proximity to a nearby filament, suggesting a more quenched population compared to galaxies in voids (Alpaslan et al. 2016). Furthermore, studies such as Kuutma, Tamm & Tempel (2017), who investigated how galaxy properties vary with distance from filament spines, found that there is an increase in the $g-i$ colour index, indicative of an aging and reddening population with declining sSFR. This trend was supported by Kraljic et al. (2018), who examined GAMA galaxies at $0.03 \leq z \leq 0.25$ and found that the fraction of red galaxies increases with proximity to filaments, independent of their distance to galaxy clusters. Moreover, the star-forming population within filaments exhibits a decreasing sSFR at fixed mass, suggesting environmental quenching. Denser filaments also host a higher proportion of early-type galaxies, supporting the morphology–density relation observed in clusters at lower redshifts (Dressler 1980) and indicating that morphological transformations can occur before galaxies enter cluster environments (e.g. Castignani et al. 2022). Similar trends have also been reported by several other studies, including Chen et al. (2017), Laigle et al. (2018), Winkel et al. (2021), and Donnan, Tojeiro & Kraljic (2022), further reinforcing the role of filamentary environments in shaping galaxy evolution.

Nevertheless, some studies provide results which are contrary to the findings described in the previous paragraph. Some studies found that the proximity of galaxies to filaments can also enhance SF activity in galaxies, which also corresponds to the increase in the fraction of star-forming galaxies (SFGs) in filaments. For example, Coppin et al. (2012) explored a system of three galaxy clusters at $z = 0.9$ and found a long filament of infrared (IR)-bright galaxies of about 2.5 Mpc in length. They recorded that this IR filament hosts a SFR of $\sim$900 $\mathrm{M_\odot\ y^{-1}}$ that was derived from its IR luminosity, L_{IR}. This SFR is relatively high compared to the normal SFR of spiral galaxies of about 1 to 10 $\mathrm{M_\odot\ y^{-1}}$ and it resembles that intermediate-density environments like filaments can also enhance the SF activity by assembling significant stellar masses in the environment. Furthermore, using a sample of 425 narrow-band selected Hα emitters, along with 2846 colour–colour selected underlying SFGs for the large-scale structure (LSS) at $z = 0.84$ in the COSMOS field, Darvish et al. (2014) found that the fraction of Hα emitters varies with environment, but shows an enhancement in filamentary structures at $z \sim 1$. This picture has also been supported by several authors, such as Liao & Gao (2019) and Vulcani et al. (2019).

From simulations' point of view, the picture whether the SF activity in galaxies is either quenched or enhanced also shows controversial results. By using a large-scale hydrodynamical cosmological simulation, the Horizon AGN simulation analysed more than 150 000 galaxies per time in the redshift range of $1.2 \leq z \leq 1.8$ and investigated the properties of galaxies, such as stellar mass and their sSFR (Dubois et al. 2014). They argued that the properties of massive galaxies show a strong source of feedback, such as active galactic nuclei (AGN), is mandatory to quench *in situ* SF and promote various morphologies. Meanwhile, Xu et al. (2020) used the EAGLE simulation to study the dependence of the galaxy properties on cosmic web environments, including filaments, and found that central galaxies which have masses below a characteristic mass of $1.8 \times 10^{10}\ h^{-1}\ \mathrm{M_\odot}$ appear redder and show lower sSFR, even though the cosmic environmental dependence is either reverse or vanish for central galaxies of masses above this characteristic mass. In addition, Malavasi et al. (2022) made use of the IllustrisTNG simulation, and coupled with the DisPerSE cosmic web extraction algorithm (Sousbie 2011), and provided a comprehensive analysis of the relation between galaxy properties and the LSS. Their results show the strongest variation with distance from the cosmic web features, more specifically, the sSFR of galaxies is generally reduced with proximity to nodes and filaments, showing that these galaxies are quenched in their SF activity. This picture has also been supported by the more recent work by Hasan et al. (2023), where they also used IllustrisTNG and DisPerSE, and found that galaxies at distances less than 1 Mpc from the filament spine have significantly suppressed SFR for galaxies with masses $8 < \mathrm{M_\star/M_\odot} < 9$, suggesting gradual gas starvation in intermediate-density environments near filaments.

On the other hand, a number of other simulation works have arrived at different conclusions, suggesting that the presence of filamentary structures within the cosmic web may actually enhance SF. For instance, Kotecha et al. (2022) conducted a study using 324 simulated clusters from The Three Hundred project, employing the DisPerSE algorithm to analyse the spatial relationships between galaxies and filaments. Their findings revealed that galaxies located near filaments within these clusters are more likely to be star-forming, exhibit bluer colours, and possess greater amounts of cold gas than their counterparts situated farther from filaments. This evidence stands in contrast to the findings discussed in the previous paragraphs, which suggested a different influence of filaments on galaxy properties. Similarly, a study by Zheng et al. (2022) supports the notion that filaments can play a significant role in enhancing SF. In their work, Zheng et al. (2022) used the Auriga simulations to examine the effects of filaments on galaxy formation within dwarf DM haloes. Their

results demonstrated that dwarf galaxies embedded within filaments tend to have higher baryonic and stellar fractions. Moreover, for a given parent halo mass, these filament-associated dwarf galaxies were found to have slightly elevated SFR compared to those residing in more isolated, field environments. These findings collectively underscore the potential influence of filaments in promoting SF, particularly in certain populations of galaxy.

The interplay between observational and simulation-based studies has yielded conflicting results, leaving the role of filaments in either quenching or enhancing galaxy activity, particularly SF or AGN activity, unclear. Although the majority of previous findings have been derived from optical or IR observations, the investigation of these effects across multiple wavelengths is crucial to develop a holistic understanding on galaxy evolution, especially to provide supports to the aforementioned previous works whether these galaxies either quench or enhance their activity in filaments. Radio observations, in particular, are invaluable as they offer insights into the dominant mechanisms driving radio emission in galaxies, whether their radio emission is either dominated by star-forming regions in SFGs or supermassive black holes at the core of AGN. By distinguishing the sources of radio emission by using radio observational probes, radio studies can complement optical and IR data to provide a more nuanced perspective on the evolutionary processes of galaxies residing in filaments.

One of the widely used probes to distinct between the SFGs and AGN population in filaments from radio observations is by using the radio source counts. Studies of 1.4 GHz radio source counts have demonstrated that typical SFGs exhibit flux densities ranging from a few μJy to a few mJy, usually up to 1 mJy, with their integrated luminosities primarily spanning from 10^{19} to 10^{24} W Hz^{-1} and peaking around 10^{22} W Hz^{-1} (e.g. Condon 1989, 1992; Garrett et al. 2000; Mauch & Sadler 2007). In contrast, AGNs typically display higher flux densities, ranging from a few mJy, usually 1 mJy, to several hundred mJy (e.g. Becker, White & Helfand 1995; Condon et al. 1998), with integrated luminosities extending from 10^{19} to 10^{27} W Hz^{-1}, dominating above $L_{1.4\ \mathrm{GHz}} = 10^{23}$ W Hz^{-1} (Matthews et al. 2021). In some other works, AGN can also start to dominate the source counts from 0.5 mJy, whereas SFGs start to dominate below 0.1 mJy (e.g. Bonzini et al. 2013; Prandoni et al. 2018; Mauch et al. 2020). The difference in the flux density threshold on the source count plots to distinguish between the SFG and AGN populations might arise from the sensitivity of different surveys. However, the flux density threshold of 1 mJy is widely used (e.g. Padovani et al. 2015; D'Amato et al. 2022), and will be also used in this work. This clear demarcation highlights the necessity of distinguishing between SFGs and AGN to accurately interpret the composition and evolution of radio source populations. In this first paper of the series, the source count will be used as the primary probe to investigate whether our sample is dominated by SFGs or AGN, and how these populations behave in filamentary structure environments by incorporating the cross-matching procedures from other wavebands too.

We organize this paper as follows: Section 2 describes the related surveys and catalogues used, as well as the segregation of samples and sub-samples considered in this work. Results and analyses which include the construction of radio source counts for all samples and sub-samples described in Section 2 is available in Section 3. The section also contains the comparison between the source counts of the samples and sub-samples from this work and from other radio sky surveys. The discussion and conclusions are given in Section 4, where the section also provides some suggestions for future works that will be discussed in the preceding papers of the series. Throughout this work, we assume the following cosmological parameters: $H_0 = 70$ km s^{-1} Mpc^{-1}, $\Omega_M = 0.3$ and $\Omega_\Lambda = 0.7$. We also use a spectral index, α, in $S \propto \nu^{\alpha}$, as –0.8.

2 SAMPLE SELECTION

This work used several well established and previously published catalogues to achieve its objective of understanding the role of filaments in shaping the evolution of radio galaxies, particularly by investigating the properties of radio galaxies within filaments located up to a certain redshift. The primary data sets include: (1) the Rapid ASKAP Continuum Survey (RACS; McConnell et al. 2020), which provides extensive radio continuum data essential for identifying and characterizing the radio emission of galaxies; (2) the Wide-field IR Survey Explorer (WISE; Wright et al. 2010), which provides IR data crucial for studying the dust-obscured SF and AGN activity in galaxies, as well as to provide photometric redshift of galaxies. (3) the SuperCOSMOS All-Sky Galaxy Survey catalogue (SCOS; Peacock et al. 2016), which offers optical imaging data that support morphological and photometric analyses; and (4) the Sloan Digital Sky Survey Data Release 16 (SDSS DR16; Blanton et al. 2017), which delivers high-resolution optical spectroscopy and imaging to facilitate the reconstruction of filaments.

By integrating these multiwavelength data sets, this work aims to determine whether filaments promote or suppress galaxy activity, with a particular focus on distinguishing between SFGs and AGN by cross-identifying them with catalogues of different wavebands. The cross-matching of these data sets is collectively referred to as the RAWS Project, and the final compiled sample resulting from this effort will be known as the RAWS sample. A brief description of the RACS, WISE, SCOS, and SDSS is given in the following subsections, and the final subsection discusses the RAWS samples.

2.1 RACS

The RACS survey is the first large-scale radio sky survey in the Southern Hemisphere conducted using the Australian Square Kilometre Array Pathfinder (ASKAP). The survey uses 903 individual pointings with 15-min observations, leveraging ASKAP's large instantaneous field of view of about 31 deg^2. It has three different observing bands, and each observing band centred at radio frequencies of 887.5 MHz (RACS-low), 1367.5 MHz (RACS-mid), and 1655.5 MHz (RACS-high). The full description of RACS-low and RACS-mid surveys is given in Hale et al. (2021) and Duchesne et al. (2023), respectively. The data reduction, imaging process, and source catalogue release of the RACS-high survey are currently undergoing and will only be made available in future papers. For the purpose of this work, the RACS-low and RACS-mid survey data releases were used, and a brief description of these two surveys is given below.

2.1.1 RACS-low

The RACS-low survey has a central frequency of 887.5 MHz, covering a large contiguous area spanning declinations (δ) from -80° to $+30^\circ$ with 799 individual tiles. This is equivalent to the total surveyed area of ∼36 200 deg^2. The observations were conducted over multiple epochs in 2019 and 2020, each with 15-min exposure times, and resulted in raw visibility data. These data were processed using the ASKAPSoft pipeline (Wieringa, Raja & Ord 2020), which converted raw visibility data into calibrated radio images. To ensure a uniform flux density scale and resolution, these radio images were

convolved to a common 25 arcsec beam size before being mosaiced into a contiguous data set. Systematic corrections were applied based on holography measurements to account for variations in ASKAP's primary beam responses. The final mosaic image of the RACS-low survey has a resolution of ∼15 arcsec.

The detection of sources in the final mosaic image was carried out using PyBDSF (Mohan & Rafferty 2015) and the detection has produced a catalogue of detected radio sources. The catalogue of the RACS-low survey achieves a 95 per cent detection rate for point sources with integrated flux densities around 5 mJy, corresponding to an overall 95 per cent completeness at approximately 3 mJy for typical sky models. The final catalogue of the RACS-low survey consists of both Gaussian component and source catalogues, distinguishing between individual radio structures and their constituent components. However, only the source catalogue had been selected to fit the purpose of this work. This is because source catalogue provides a simplified representation of radio sources, while the Gaussian component catalogue captures detailed structures, which the source catalogue is better suited for general astrophysical studies, such as AGN demographic and SFG counts. The RACS-low data release source catalogue contains 2123 638 radio sources and excludes the region within $|b| < 5^{\circ}$ around the Galactic plane (Hale et al. 2021).

2.1.2 *RACS-mid*

Following the work by Hale et al. (2021) on the RACS-low survey, Duchesne et al. (2023) later published a paper that focuses on the second data release of the RACS survey at 1367.5 MHz, which later to be known as the RACS-mid survey. The RACS-mid survey has a resolution of ∼10 arcsec, which provides an improved resolution compared to the RACS-low survey. The raw visibility data of the RACS-mid survey had also been imaged by using the same procedures as in RACS-low survey, and the final mosaic images produced were divided into three different categories for different future scientific purposes. These categories include the primary, 25 arcsec and time-domain calibrated images. However, this work focuses on the use of the RACS-mid 25 arcsec final mosaic image for further analysis. The 25 arcsec full-sensitivity images (and the corresponding catalogue) are limited to declinations of $\delta = +30^{\circ}$, similar to RACS-low, because the point spread function major axis in some original images exceeds 25″ beyond this declination. In cataloguing the RACS-mid data release of the three different categories of images, including the RACS-mid 25 arcsec final mosaic image, Duchesne et al. (2023) adopted the same procedures established for constructing the RACS-low catalogue, as described in Hale et al. (2021).

Since the source detection analysis involved three categories of final mosaic images, the images of the RACS-mid survey have produced three key source and component catalogues, which include the primary, 25 arcsec, and time-domain catalogues. However, as described in the previous paragraph, the 25 arcsec catalogue had been used for the purpose of this work. This is because the catalogue provides a matched 25 arcsec resolution, aligning with the RACS-low coverage to facilitate direct comparisons with lower frequency observations. The catalogue was constructed in the same way as the RACS-mid primary catalogue, but the images were convolved to a lower, less-sensitive angular resolution of 25 arcsec. Even though the 25 arcsec catalogue has a lower sensitivity compared to the RACS-mid primary catalogue due to increased source blending, the catalogue is found to be 95 per cent complete at 2.5 mJy, which suggests that the catalogue can go deeper and pick up fainter sources down to 2.5 mJy compared to that of the RACS-low catalogue, which can detect sources down to 3 mJy. The source catalogue of the 25 arcsec catalogue consists of 1990 598 radio sources after subtracting sources that lie in the region within the Galactic plane.

2.2 WISE × SCOS

Searching for the redshift information of the RACS radio sources is important to reveal their distance information and, therefore, to position them in the three-dimensional sky coverage of the respective filaments later. Since the catalogues of radio sources in the RACS surveys do not contain redshift information, it was necessary to cross-match these radio sources with any spectroscopic or photometric redshift galaxy surveys. For this reason, the SCOS survey was chosen to carry out this task, since it covers all sky coverage with more than 240 million objects available in the catalogue. However, the raw catalogue of the SCOS survey (Peacock et al. 2016) contains many objects that are, in fact, blends of stellar images and also does not contain distance information for many of these objects.

Cross-identifications with IR data from the WISE all-sky data release are quite a solution to both problems (Wright et al. 2010). The data release includes the WISE × SCOS Photometric Redshift catalogue, created by cross-matching the ALLWISE and SCOS data sets and utilizing the artificial neural network-based ANNz algorithm (Collister & Lahav 2004), which was trained on data from the GAMA-II redshift survey (Driver et al. 2011; Liske et al. 2015). The resulting photometric redshifts exhibit errors that are largely independent of distance, achieving an overall accuracy of $\sigma_z/(1 + z) = 0.033$, with a minimal fraction of outliers. These redshift estimates have a typical precision of 15 per cent. The WISE × SCOS sample, following appropriate masking, comprises approximately 18.5 million galaxies with a median redshift of $z = 0.2$ (Bilicki et al. 2016).

2.3 SDSS

In order to identify whether or not the cross-matched sources between RACS and WISE × SCOS are located in any filaments, it was required to reconstruct filaments by also making use of any spectroscopic or photometric redshift galaxy surveys. However, the reconstruction of filaments could also be done by using any available catalogues of filaments. After having searched for the catalogues, this work had selected the cosmic filament catalogue that was produced by Carrón Duque et al. (2022). Their catalogue was produced by using the data taken from the SDSS DR16. By using the SDSS DR16 data, Carrón Duque et al. (2022) reconstructed filaments as one-dimensional maxima in the galaxy distribution and their filament reconstruction covers redshifts up to $z = 2.2$. In particular, they used two subsurveys from the SDSS survey, which are the Baryon Oscillation Spectroscopic Survey (BOSS) and the extended BOSS (eBOSS), where these subsurveys were divided into different subsamples based on different redshift ranges.

Taking advantage of the final SDSS DR12, Dawson et al. (2012), Anderson et al. (2014), and Alam et al. (2015) divided the BOSS survey into the LOWZ and CMASS subsamples, where the redshift range of these subsamples was defined as $0.05 \leq z \leq 0.5$ and $0.4 \leq z \leq 0.8$, respectively. Carrón Duque et al. (2022) used both of these samples in their filament reconstructions, but for the purpose of this work, the maximum range of redshifts covered is $0.564 \leq z \leq 0.57$. This redshift limit ensures consistency with the redshift coverage over which optical counterparts to RACS sources have

Table 1. The list of samples considered in this work, which include all RAWS, RAWS non-filament, and RAWS filament galaxies. Note that the number of radio galaxies given in columns (2) and (5) is the number of radio galaxies after the cross-matching procedure with the RACS, ALLWISE × SCOS, and SDSS16 for both samples, RAWS-low and RAWS-mid samples, respectively.

Samples	RAWS-low			RAWS-mid		
	N	Redshift range	Ω (deg^2)	N	Redshift range	Ω (deg^2)
(1)	(2)	(3)	(4)	(5)	(6)	(7)
All RAWS galaxies	120 543	$0.0015 \leq z \leq 0.5681$	1738	110 741	$0.0015 \leq z \leq 0.5591$	1721
RAWS non-filament galaxies	39 123	$0.0015 \leq z \leq 0.5681$	431	36 494	$0.0015 \leq z \leq 0.5591$	422
RAWS filament galaxies	9095	$0.0503 \leq z \leq 0.5423$	359	8975	$0.0503 \leq z \leq 0.5423$	352

reliable spectroscopic redshifts, which is critical for accurate filament identification. Beyond this range, the completeness of spectroscopic surveys like BOSS decreases, making filament reconstruction less reliable. As a result, this work includes the entire LOWZ sample and approximately half of the CMASS sample. Within this range, filaments across 98 redshift bins have been reconstructed. A detailed description of the cosmic filament reconstruction process is provided in Carrón Duque et al. (2022).

2.4 The RAWS Sample

To facilitate clarity in referencing, we define the cross-matched samples used in this work as RAWS-low and RAWS-mid samples. Specifically, the RAWS-low sample refers to the set of sources obtained by cross-matching the RACS-low radio survey with the combined ALLWISE × SCOS optical-IR catalogue. Similarly, the RAWS-mid sample represents the result of cross-matching the RACS-mid survey with the same ALLWISE × SCOS data set. This naming convention allows for consistent identification of the samples used for subsequent statistical and environmental analysis. Given that the RACS sources in these samples possess associated optical counterparts through this cross-matching procedure, they are interpreted as radio galaxies within the context of this work.

To identify the optical counterparts of RACS radio sources in both the RAWS-low and RAWS-mid samples, we cross-matched the RACS source positions with optical and IR data from the WISE and SCOS surveys. Given that the SCOS data set offers a positional resolution of approximately 2 arcsec and WISE provides a lower resolution of about 6 arcsec, we adopted a conservative matching radius of 6 arcsec for the RAWS samples. This threshold accounts for the varying positional uncertainties between the optical, IR, and radio data, while also aligning with the angular resolution of the RACS surveys. By choosing this offset, we ensure that the matching process accommodates the resolution limits of both WISE and SCOS, thereby maximizing the reliability of the identified counterparts without significantly increasing the likelihood of false associations.

Carrón Duque et al. (2022) describe cosmic filaments as sequences of discrete points along spine-like structures reconstructed within tomographic redshift slices. Each point on the filament spine is associated with a local positional uncertainty, which quantifies the confidence in the filament's angular location and serves as a proxy for the filament's transverse extent. This uncertainty can be interpreted as the spatial boundary around the spine within which a galaxy may be considered physically associated with the filament.

In this work, we use these positional uncertainties to determine the filament membership of RAWS galaxies. The process begins by segregating the RAWS galaxies according to the redshift bins used in the filament reconstruction. For each redshift slice, we evaluate the angular separation between each RAWS galaxy and the nearest point along the corresponding filament spine. A galaxy is classified as a filament member if its projected separation falls within the local uncertainty envelope defined for that spine segment. This approach allows us to assign filament membership in a manner that accounts for both the redshift localization of the filaments and the spatial confidence limits associated with their detection.

3 RESULTS AND ANALYSIS

The results and analysis presented for the RAWS-low and RAWS-mid samples are discussed in the context of their contribution to fulfilling the main objectives of this work. The number of RAWS galaxies classified by environment (filament or field) is summarized after the cross-matching process between the RACS and WISE × SCOS catalogues. Visual maps that show the spatial distribution of RAWS galaxies overlaid on reconstructed filaments, highlighting differences between the two samples, are also given. Due to redshift uncertainties, a probability method was used to improve filament membership assignment of RAWS galaxies. Finally, source count plots reveal that RAWS galaxies in filaments, or RAWS filament galaxies, are less numerous than those in the field, and statistical tests confirm that their flux distributions are significantly different.

3.1 RACS and WISE × SCOS cross-matching

Following the cross-matching procedure between the RACS and WISE × SCOS catalogues, as detailed in Section 2.4, we obtained the final, clean sample of RAWS galaxies to be used for the subsequent source count analysis. Table 1 provides a summary of the number of radio galaxies identified in both the RAWS-low and RAWS-mid samples. It also categorizes these galaxies based on their spatial association with large-scale structures, particularly filaments, along with their effective filament areas. The table distinguishes between the total number of cross-matched radio galaxies for both samples, those that do not reside within any filamentary structures, and those that are associated with filaments, as defined by filamentary structure reconstructions of Carrón Duque et al. (2022).

From the total number of all RAWS galaxies for both samples described in Table 1, we also examine for any possibilities whether the RAWS galaxies in our samples contain multiple matches within a conservative matching radius of 6 arcsec. This examination was necessary to ensure the reliability of the cross-matching process. Multiple optical counterparts within the 6 arcsec search radius can lead to ambiguous associations, which may affect redshift accuracy and environmental classification. By identifying and quantifying such cases, we confirm that the majority of RAWS galaxies have unique matches, supporting the robustness of the final sample used in our analysis. To check whether or not the RACS sources have multiple matches in 6 arcsec matching radius, we performed a closest neighbour cross-matching with the WISE × SCOS photometric redshift catalogue and calculate the mean distance to their closest

neighbours. The matching process was based primarily on angular proximity, selecting the closest WISE × SCOS galaxy within this radius as the most likely counterpart for each RACS source.

Although a small fraction of RACS sources are found to have multiple WISE × SCOS galaxies within the 6 arcsec search radius, the overall occurrence of such cases remains minimal. Table 2 shows the summary of the statistics of the cross-matching between RACS radio sources and WISE × SCOS galaxies, for the nth closest neighbour. The percentages of RAWS-low and RAWS-mid galaxies that contain multiple WISE × SCOS galaxies within our search radius are only 1.4 per cent and 1.2 per cent, respectively, hence, suggesting that more than 98 per cent of the data set contain only one WISE × SCOS counterpart within the 6 arcsec search radius. We also checked the same statistics in the filament galaxies, and found a consistent result, where the fraction is less than 2 per cent, compared to the entire RAWS catalogue. In both cases, we found that the mean distance to the first and second neighbours are 2.36–2.46 arcsec and 4.53–4.86 arcsec, respectively. As every RAWS galaxy has a clearly identified first-nearest neighbour, the presence of a small number of multiple matches does not compromise the integrity of the source count analysis. The source counts presented in this work incorporate the full RAWS sample as summarized in Table 1, ensuring that all matched RAWS galaxies are accounted for consistency.

3.2 Filament assignment

After ensuring the uniqueness of cross-matched associations, the RAWS galaxies were overlaid on to the corresponding filament reconstructions within their corresponding redshift bins. Fig. 1 shows two examples of the reconstructed filaments in a redshift range of $0.249 \leq z \leq 0.255$ for RAWS-low (top panel) and RAWS-mid (bottom panel) samples, along with the injected radio galaxies. In both panels, the reconstructed filaments are represented by grey regions, while the radio galaxies are shown as dots, in such a way that radio galaxies residing in filaments are represented by red dots, and we define these radio galaxies as filament galaxies. Meanwhile, the black dots are those radio galaxies located outside of filaments (or in fields) and will be known as non-filament galaxies. This classification highlights the distinction between radio galaxies that trace the large-scale structure of filaments and those that exist in the more sparsely populated field regions.

As mentioned in Section 2.2, the WISE × SCOS photometric catalogue (Bilicki et al. 2016) provides redshift values with typical uncertainties relatively larger than the SDSS filament catalogue redshift bin sizes, i.e. $\Delta z \sim 0.005$–0.008, and allows for the possibility that the RAWS galaxy may fall into multiple redshift bins, which further complicates the filament membership assignment. To quantify this matter, we calculated the redshift likelihood for each RAWS galaxy based on a Gaussian probability distribution function, weighted by the presence of filaments. On average, the RAWS filament galaxies have significantly higher chances of residing in filaments compared to RAWS field galaxies, which strengthens our claims that RAWS filament galaxies are indeed associated within a filament, regardless of which redshift bin that these RAWS galaxies belong to.

Note that Fig. 1 shows a full-scale of the reconstructed filaments along with the radio galaxies, but to get a closer view of this structure, we also provide the zoom-in images of this structure, as shown in Fig. 2. Similar to Fig. 1, the top and bottom panels of Fig. 2 show the filamentary structure in a redshift range of $0.249 \leq z \leq 0.255$, with the top panels are for the RAWS-low sample and the bottom panels are for the RAWS-mid sample. All four panels have the same declination range, where they extend from 0° to 15°. However, each panel of the samples has a different right ascension (α) range, in which the left panels illustrate the region spanning $185° \leq \alpha \leq 215°$, while the right panels cover the range of $330° \leq \alpha \leq 360°$. This right ascension ranges are the same for both RAWS-low and RAWS-mid samples. The colour bars, which correspond to the colours of the filaments, represent the estimated uncertainty of the detection in degrees, measured by using methods described in Carrón Duque et al. (2022). In Fig. 2, the colours of filament and non-filament radio galaxies follow the same colour-code as in Fig. 1.

In addition, Fig. 2 offers a detailed visualization of the spatial distribution of radio galaxies within the RAWS-low and RAWS-mid samples, enabling a comparative analysis of their association with cosmic filaments across different regions of the sky. Notably, while some radio galaxies appear in both the RAWS-low and RAWS-mid samples, others are exclusive to one data set only. For instance, the top-left panel of Fig. 2 displays 33 filament-associated galaxies, whereas the bottom-left panel shows 34 such galaxies. A subset of these filament galaxies is common to both panels, but some are uniquely detected in either the RACS-low or RACS-mid survey. This variation is primarily due to differences in sensitivity, resolution, or noise characteristics between the two surveys, which affect the detectability of certain sources. Although certain radio sources are present in both the RACS-low and RACS-mid catalogues, and some are not, slight discrepancies in detection between the two can lead to differences in filament association. However, these discrepancies are not significant and do not introduce systematic errors into the subsequent analysis.

3.3 Source counts

As mentioned in Section 1, the primary objective of this work is to construct source count plots for the radio galaxies listed in Table 1. In line with this aim, it was necessary to extract the radio flux density measurements from the catalogues of the RACS-low and RACS-mid surveys. These surveys provide initial flux density measurements for the radio sources at frequencies of 887.5 and 1367.5 MHz, respectively, reflecting the observing frequencies of the RACS-low and RACS-mid data sets. To ensure consistency in the comparative analysis with results from other surveys, these flux density values were subsequently rescaled to correspond to a reference frequency of 1.4 GHz by using the relationship below:

$$\ln \frac{S_\nu}{S_{1.4}} = \alpha \ln \frac{1.4}{\nu}, \tag{1}$$

where S_ν is the flux density of a radio galaxy observed in a certain frequency, ν, and α is the spectral index – the value of α is defined in Section 1. Since this work uses two RACS surveys, ν is defined as the central frequency of RACS-low and RACS-mid surveys, which is 887.5 and 1367.5 MHz, respectively. This rescaling provides a standardized approach for comparing the radio galaxy populations across different studies and survey data sets, as 1.4 GHz serves as a common reference frequency for many radio surveys. The converted 1.4-GHz flux densities for radio galaxies in both samples will be used to construct source count profiles for all RAWS galaxies, RAWS filament galaxies and RAWS non-filament galaxies, with a complimentary source count of the RACS-low and RACS-mid radio sources as reference.

A source count, which is defined as the number of sources per unit of steradian (Ω), was calculated for each flux density bin and subsequently normalized by dividing it by the width of the bin

Table 2. Summary of the statistics of the cross-matching between RACS and WISE × SCOS that contributes to the final RAWS sample. Each row lists the number of sources (N) and the average distance ($\bar{d}$) of the nth neighbour for RACS radio sources with at least n WISE × SCOS neighbour(s).

	RAWS-low				RAWS-mid			
	All		Fil. galaxies		All		Fil. galaxies	
n	N	$\bar{d}$	N	$\bar{d}$	N	$\bar{d}$	N	$\bar{d}$
1	120 543	2.46 arcsec	9095	2.39 arcsec	110 741	2.45 arcsec	8975	2.44 arcsec
2	1655 (1.4 per cent)	4.49 arcsec	140 (1.5 per cent)	4.86 arcsec	1382 (1.2 per cent)	4.53 arcsec	118 (1.3 per cent)	4.66 arcsec
3	6 (0.005 per cent)	4.60 arcsec	0	–	7 (0.006 per cent)	5.24 arcsec	1 (0.011 per cent)	5.73 arcsec
4	0	–	0	–	1 (∼0 per cent)	5.63 arcsec	0	–

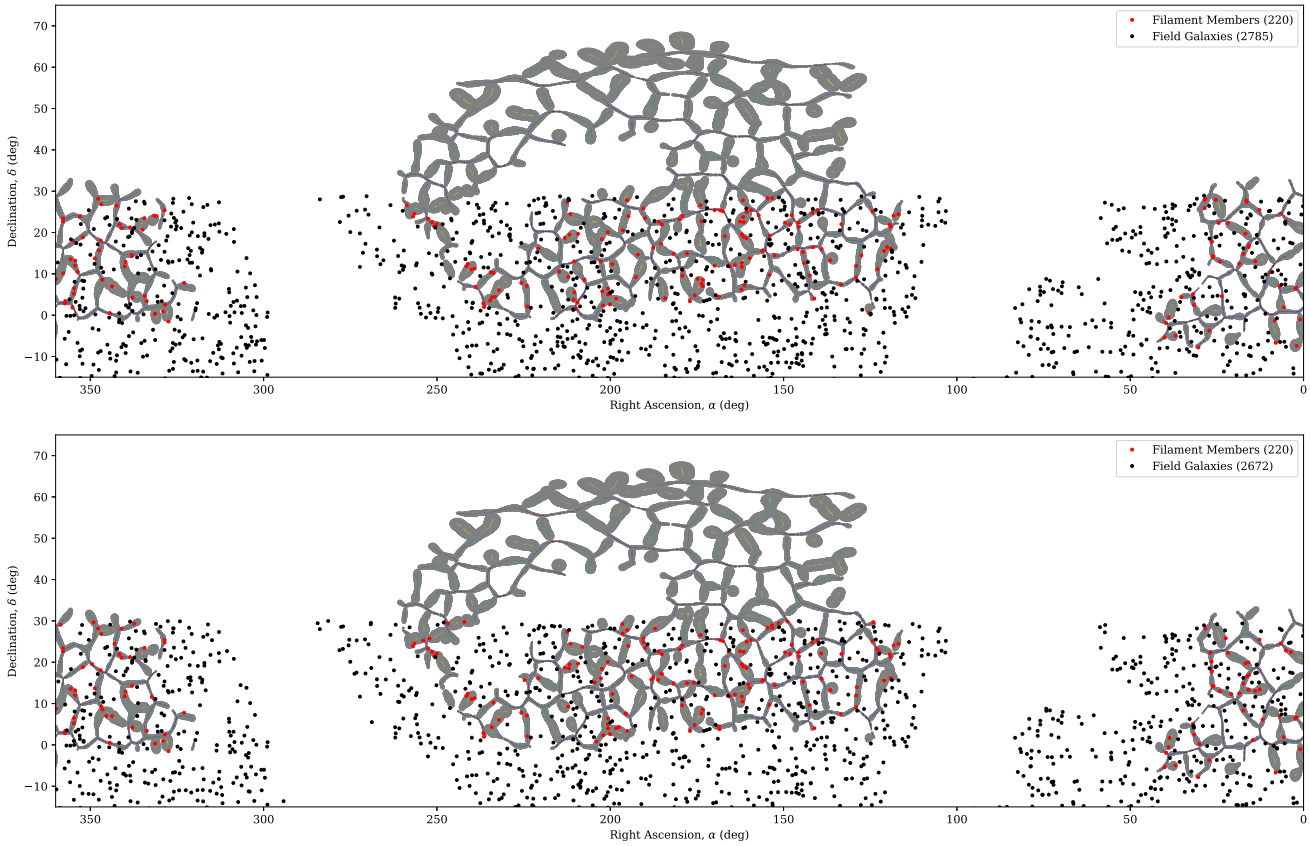

Figure 1. Examples of filamentary structure obtained by reconstructing them following procedures described in Carrón Duque et al. (2022). Both panels show filaments in a redshift bin $0.249 < z < 0.255$. The top panel shows the filament reconstruction along with the RACS radio sources for the RAWS-low sample, while the bottom panel indicates the same features, but for the RAWS-mid sample. The RAWS filament and non-filament galaxies are represented by the red and black dots, respectively.

(expressed in Jy). This value was then divided by a flux-density-weighted average, $S^{5/2}$, to compute the Euclidean-normalized differential source counts, $S^{5/2}\,\mathrm{d}N/\mathrm{d}S$, with units of $\mathrm{Jy}^{1.5}\ \mathrm{sr}^{-1}$. The average flux density, $\bar{S}$, for each bin was determined using the following expression:

$$\bar{S} = \frac{\int_{S_\mathrm{l}}^{S_\mathrm{u}} S\left(\frac{\mathrm{d}N}{\mathrm{d}S}\right)\mathrm{d}S}{\int_{S_\mathrm{l}}^{S_\mathrm{u}} \left(\frac{\mathrm{d}N}{\mathrm{d}S}\right)\mathrm{d}S}, \tag{2}$$

where S_l and S_u denote the lower and upper bounds of the flux density bin, respectively (Henkel & Partridge 2005). This approach ensures a consistent normalization across flux intervals, allowing for direct comparison of source counts across different surveys and flux regimes. The RAWS-low and RAWS-mid samples were divided into three subsamples, so that each sample has all galaxies, filament galaxies and non-filament galaxies subsamples. Based on the number of radio galaxies and sky coverage listed in Table 1, the source counts of the RAWS-low and RAWS-mid subsamples were being quantified, and the values are given in Table 3. Note that Table 3 only shows the counts in the first 30 bins of the RAWS-low and RAWS-mid subsamples, respectively, and the complete table can be found in the online supplementary material of this paper. The errors shown in Table 3 are Poissonnian, and the determination of the errors was calculated using methods described in Gehrels (1986). Also note that the sky coverages shown in Table 1 are the effective sky coverage based on the matching rate between their respective RACS and WISE × SCOS catalogues, which provides a representation of the sky coverage that RACS would have, only surveying regions with optical counterparts. The filament area is obtained based on the stacked sky coverage in all redshifts, while the *field*/non-filament area is calculated based on the area not covered by the filament catalogue, with the declination limited to RACS and SDSS coverage.

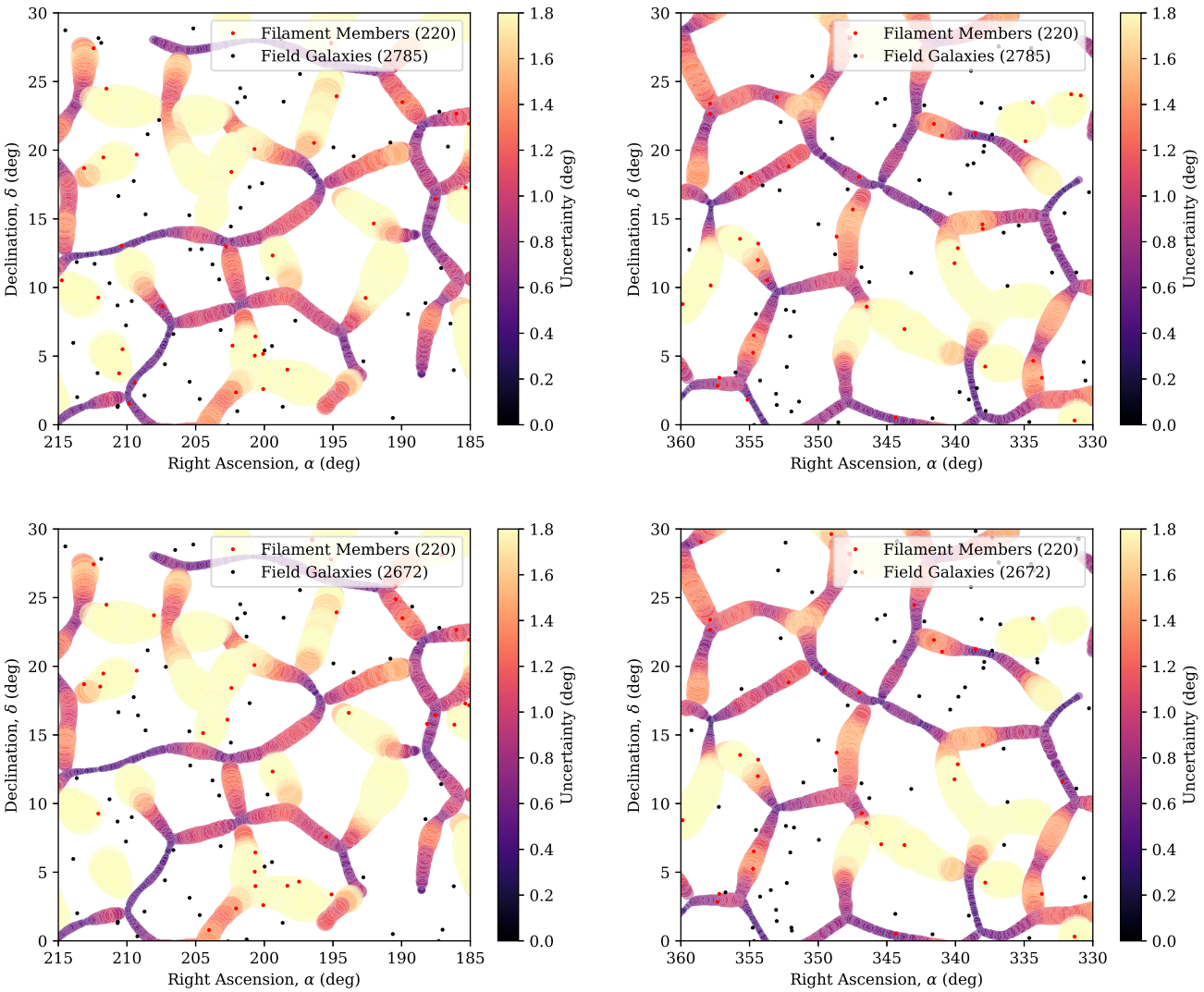

Figure 2. The zoom-in images of filaments shown in Fig. 1. While all panels show the same redshift bin of $0.249 < z < 0.255$ and of declination between 0° and +30°, the top panels show the distribution of the RAWS-low galaxies and the bottom panels show the distribution of the RAWS-mid galaxies. However, the left panels represent right ascensions between 185° and 215°, and the right panels indicate right ascensions between 330° and 360°. The colour bars indicate the estimated detection uncertainty in degrees, as determined using the methodology outlined by Carrón Duque et al. (2022).

The source counts of the RAWS-low and RAWS-mid subsamples were then plotted based on the counts shown in Table 3, respectively. The plots of the source counts of the subsamples are given in Fig. 3. The top panel shows the source count plots for all subsamples of the RAWS-low sample. Meanwhile, the source count plots for all subsamples of the RAWS-mid sample are shown in the bottom panel of the figure. In both panels, the colour code for the data points of the source counts follows the colour code shown in Figs 1 and 2 with additional data points for all RAWS galaxies – denoted by blue filled circle. The plots also include the source counts for all sources from RACS-low and RACS mid data releases, in which they are represented by grey filled circles. The error bars for all subsamples in both panels are also shown in the plots, following the errors presented in Table 3.

To provide comparison with the source counts from previous radio sky surveys at 1.4 GHz, the 1.4-GHz normalized-Euclidean source count plots from this work were also overlaid on the source counts from those surveys, as also shown in Fig. 3. Those radio sky surveys include the LAST-FIRST survey (Helfand, White & Becker 2015; indigo line), the ATESP survey (Prandoni et al. 2001; red line), the FIRST survey (White et al. 1997; orange line), the Lockman Hole Project survey (Prandoni et al. 2018; lime line), the MIGHTEE-COSMOS survey (Hale et al. 2022; turquoise line), the VLA-COSMOS survey (Bondi et al. 2008; blue-violet line), and the VLBA+BGT-COSMOS (Herrera Ruiz et al. 2018; magenta line) survey. The colour-filled region around the line of these radio sky surveys indicates the uncertainty range around their respective source counts.

A careful inspection of both panels in Fig. 3 reveals a noticeable flattening in the differential radio source counts at lower flux density levels, specifically below approximately 3 mJy for the RAWS-low subsample and below 2.5 mJy for the RAWS-mid subsample. This turnover is consistent with the completeness limits reported for the RACS surveys, as established by Hale et al. (2021) and Duchesne et al. (2023), and reflects the 95 per cent completeness thresholds for the respective RAWS catalogues, as stated in Sections 2.1.1

Table 3. Tabulated 1.4-GHz normalized-Euclidean source counts for the (a) RAWS-low and (b) RAWS-mid samples for the first 10 flux density bins. The first column shows the lower boundary of the flux density bin, S_l. For each sample, the source counts for all RACS radio sources, all RAWS galaxies, RAWS non-filament galaxies, and RAWS filament galaxies are presented in this table. The error bars shown in the table are Poissonian, adopted from Gehrels (1986). The complete list of this table can be found as online supplementary materials.

(a) RAWS-low sample

	RACS-low			RAWS-low			RAWS-low non-fil. gal.			RAWS-low fil. gal.		
S_l (Jy)	N	$\langle S \rangle$ ($\times 10^{-3}$ Jy)	$S^{2.5}$ dN/dS (Jy$^{1.5}$ sr^{-1})	N	$\langle S \rangle$ ($\times 10^{-3}$ Jy)	$S^{2.5}$ dN/dS (Jy$^{1.5}$ sr^{-1})	N	$\langle S \rangle$ ($\times 10^{-3}$ Jy)	$S^{2.5}$ dN/dS (Jy$^{1.5}$ sr^{-1})	N	$\langle S \rangle$ ($\times 10^{-3}$ Jy)	$S^{2.5}$ dN/dS (Jy$^{1.5}$ sr^{-1})
0.00100	64685 ± 254	1.11 ± 0.06	1.060 ± 0.004	5361 ± 73	1.11 ± 0.06	1.548 ± 0.021	1031 ± 32	1.11 ± 0.06	1.202 ± 0.037	245 ± 16	1.11 ± 0.06	0.342 ± 0.022
0.00121	108134 ± 329	1.34 ± 0.07	2.350 ± 0.007	8081 ± 90	1.33 ± 0.07	3.094 ± 0.034	1939 ± 44	1.34 ± 0.07	2.997 ± 0.068	447 ± 21	1.34 ± 0.07	0.828 ± 0.039
0.00146	146777 ± 383	1.61 ± 0.09	4.229 ± 0.011	10457 ± 102	1.61 ± 0.09	5.308 ± 0.052	2919 ± 54	1.61 ± 0.09	5.982 ± 0.111	640 ± 25	1.61 ± 0.09	1.572 ± 0.062
0.00176	169113 ± 411	1.94 ± 0.10	6.460 ± 0.016	10810 ± 104	1.93 ± 0.11	7.275 ± 0.070	3408 ± 58	1.94 ± 0.11	9.259 ± 0.159	744 ± 27	1.94 ± 0.10	2.423 ± 0.089
0.00212	175157 ± 419	2.33 ± 0.13	8.870 ± 0.021	10173 ± 101	2.33 ± 0.13	9.076 ± 0.090	3360 ± 58	2.33 ± 0.13	12.102 ± 0.209	717 ± 27	2.33 ± 0.12	3.096 ± 0.116
0.00256	169521 ± 412	2.81 ± 0.15	11.381 ± 0.028	8988 ± 95	2.81 ± 0.15	10.630 ± 0.112	3160 ± 56	2.81 ± 0.15	15.089 ± 0.268	716 ± 27	2.82 ± 0.15	4.098 ± 0.153
0.00309	157153 ± 396	3.39 ± 0.18	13.987 ± 0.035	8124 ± 90	3.39 ± 0.18	12.738 ± 0.141	2945 ± 54	3.39 ± 0.19	18.642 ± 0.344	697 ± 26	3.40 ± 0.19	5.289 ± 0.200
0.00373	141075 ± 376	4.09 ± 0.22	16.646 ± 0.044	6975 ± 84	4.10 ± 0.22	14.499 ± 0.174	2506 ± 50	4.10 ± 0.22	21.030 ± 0.420	587 ± 24	4.10 ± 0.22	5.905 ± 0.244
0.00450	125340 ± 354	4.94 ± 0.27	19.606 ± 0.055	6179 ± 79	4.94 ± 0.27	17.028 ± 0.217	2278 ± 48	4.94 ± 0.27	25.343 ± 0.531	529 ± 23	4.94 ± 0.28	7.055 ± 0.307
0.00543	110056 ± 332	5.96 ± 0.32	22.822 ± 0.069	5503 ± 74	5.97 ± 0.33	20.104 ± 0.271	2050 ± 45	5.98 ± 0.32	30.235 ± 0.668	460 ± 21	5.94 ± 0.32	8.132 ± 0.379

(b) RAWS-mid sample

	RACS-mid			RAWS-mid			RAWS-mid non-fil. gal.			RAWS-mid fil. gal.		
S_l (Jy)	N	$\langle S \rangle$ ($\times 10^{-3}$ Jy)	$S^{2.5}$ dN/dS (Jy$^{1.5}$ sr^{-1})	N	$\langle S \rangle$ ($\times 10^{-3}$ Jy)	$S^{2.5}$ dN/dS (Jy$^{1.5}$ sr^{-1})	N	$\langle S \rangle$ ($\times 10^{-3}$ Jy)	$S^{2.5}$ dN/dS (Jy$^{1.5}$ sr^{-1})	N	$\langle S \rangle$ ($\times 10^{-3}$ Jy)	$S^{2.5}$ dN/dS (Jy$^{1.5}$ sr^{-1})
0.00100	19447 ± 139	1.12 ± 0.06	0.316 ± 0.002	1457 ± 38	1.12 ± 0.06	0.425 ± 0.011	92 ± 11	1.13 ± 0.06	0.109 ± 0.013	19 ± 5	1.12 ± 0.06	0.027 ± 0.008
0.00121	58255 ± 241	1.35 ± 0.07	1.253 ± 0.005	4137 ± 64	1.35 ± 0.07	1.600 ± 0.025	384 ± 20	1.36 ± 0.07	0.606 ± 0.031	102 ± 10	1.35 ± 0.07	0.193 ± 0.019
0.00146	112869 ± 336	1.61 ± 0.09	3.219 ± 0.010	7637 ± 87	1.61 ± 0.09	3.915 ± 0.045	1140 ± 34	1.62 ± 0.08	2.384 ± 0.071	296 ± 17	1.63 ± 0.08	0.742 ± 0.043
0.00176	161906 ± 402	1.94 ± 0.10	6.122 ± 0.015	10166 ± 101	1.94 ± 0.10	6.910 ± 0.069	2452 ± 50	1.95 ± 0.10	6.797 ± 0.137	580 ± 24	1.95 ± 0.11	1.927 ± 0.080
0.00212	186629 ± 432	2.34 ± 0.13	9.355 ± 0.022	10770 ± 104	2.33 ± 0.13	9.705 ± 0.094	3324 ± 58	2.34 ± 0.13	12.215 ± 0.212	849 ± 29	2.34 ± 0.12	3.740 ± 0.128
0.00256	188810 ± 435	2.81 ± 0.15	12.548 ± 0.029	10491 ± 102	2.81 ± 0.15	12.532 ± 0.122	3746 ± 61	2.82 ± 0.15	18.250 ± 0.298	944 ± 31	2.82 ± 0.16	5.513 ± 0.179
0.00309	173391 ± 416	3.39 ± 0.18	15.276 ± 0.037	9059 ± 95	3.39 ± 0.18	14.346 ± 0.151	3470 ± 59	3.39 ± 0.18	22.412 ± 0.380	849 ± 29	3.38 ± 0.18	6.573 ± 0.226
0.00373	151933 ± 390	4.09 ± 0.22	17.745 ± 0.046	7692 ± 88	4.10 ± 0.22	16.149 ± 0.184	3041 ± 55	4.09 ± 0.22	26.038 ± 0.472	730 ± 27	4.10 ± 0.22	7.492 ± 0.277
0.00450	130516 ± 361	4.94 ± 0.27	20.209 ± 0.056	6723 ± 82	4.94 ± 0.27	18.712 ± 0.228	2648 ± 51	4.94 ± 0.27	30.058 ± 0.584	664 ± 26	4.94 ± 0.27	9.035 ± 0.351
0.00543	111580 ± 334	5.96 ± 0.32	22.904 ± 0.069	5737 ± 76	5.96 ± 0.32	21.168 ± 0.279	2269 ± 48	5.96 ± 0.32	34.145 ± 0.717	529 ± 23	5.97 ± 0.32	9.542 ± 0.415

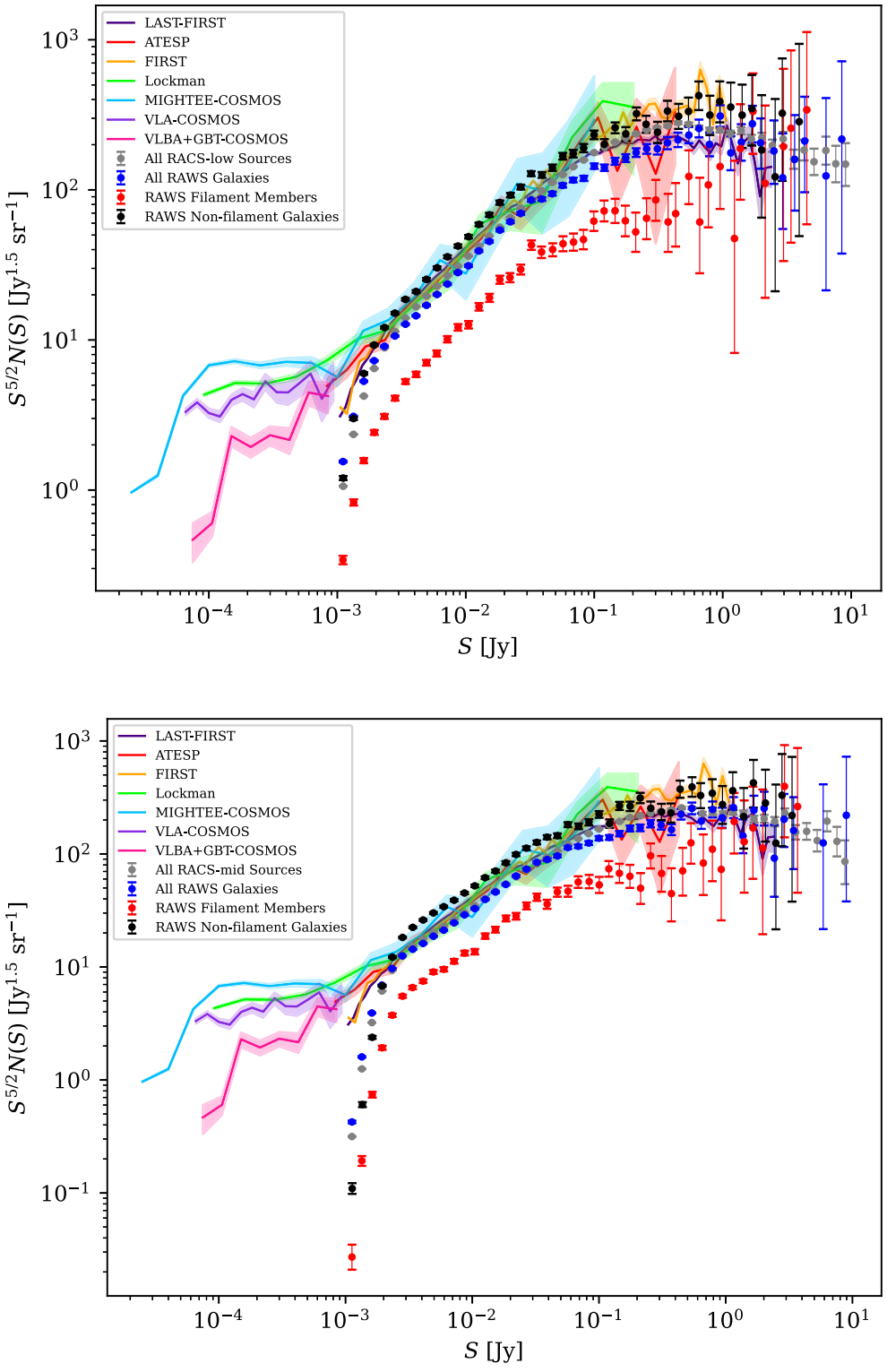

Figure 3. The 1.4-GHz normalized-Euclidean source count plots of the RAWS-low (top panel) and RAWS-mid (bottom panel) sample overlaid with the source counts from other previous radio surveys. In both panels, the colour code for the RAWS filament and non-filament galaxies is the same as in Fig. 1, with additional samples are also shown in the figure – all RACS sources (grey dots) and all RAWS galaxies (blue dots). The source counts from other previous radio surveys include the LAST-FIRST survey (indigo line), the ATESP survey (red line), the FIRST survey (orange line), the Lockman Hole Project (lime line), the MIGHTEE-COSMOS survey (turquoise line), the VLA-COSMOS survey (blue-violet line), and the VLBA+GBT-COSMOS (magenta line).

and 2.1.2 for the RACS-low and RACS-mid surveys, respectively. The observed deviation from the expected Euclidean slope at these flux density levels suggests increasing incompleteness, which is a known limitation when dealing with faint radio sources in wide-area continuum surveys. Importantly, it should be noted that the nominal flux density threshold typically used to distinguish between SFGs and AGN in radio source count studies is approximately 1 mJy. Therefore, the majority of sources included in both the RAWS-low and RAWS-mid samples are above this threshold and are thus predominantly AGN-dominated populations.

It is clear in both panels of Fig. 3 that the differential source counts for the full RAWS galaxy sample and the RAWS non-filament galaxies show strong consistency with those derived from previous large-area radio sky surveys, as evidenced by their alignment within the shaded regions that represent the source count distributions of earlier studies. This agreement, particularly across the flux density range of approximately 3–100 mJy, reinforces the reliability and completeness of both subsamples. In contrast, the source count distributions for the RAWS filament galaxies – across both the RAWS-low and RAWS-mid samples – systematically fall below those of the other RAWS subsamples and the majority of previous surveys throughout the full flux density range examined. This deviation indicates a comparatively lower surface density of radio sources, particularly AGN, within filamentary environments relative to those in non-filament or field regions, as well as those captured in blind surveys. The underabundance of filament galaxies becomes especially pronounced at flux densities exceeding the 95 per cent completeness threshold of the RACS surveys, where the influence of observational biases is minimized.

To statistically assess whether different subsamples of radio sources originate from the same underlying distribution, the Kolmogorov–Smirnov (KS) test was applied to their flux density distributions. In the context of the RAWS samples, the KS test was used to determine whether the flux density distributions of radio galaxies in filaments differ significantly from those outside filamentary environments. After applying the test to the subsamples of RAWS filament and non-filament galaxies for both RAWS-low and RAWS-mid samples, the p-values for both samples have been found to be extremely less than 0.05, i.e. 1.035×10^{-63} for RAWS-low subsamples and 2.412×10^{-75} for RAWS-mid subsamples. These p values indicate that the null hypothesis – which states that both subsamples are drawn from the same parent distribution – can be rejected at a statistically significant level. This suggests that environmental factors, such as residing in a filamentary structure, may influence the radio properties of galaxies.

4 DISCUSSION AND CONCLUSIONS

The radio source count analysis presented in this work provides direct observational evidence that complements and expands upon the environmental framework outlined in Section 1. Superclusters, as the largest gravitationally bound systems in the Universe, contain a hierarchy of structures with varying densities, including filaments – elongated, intermediate-density structures connecting clusters and groups (e.g. Tully et al. 2014; Chon et al. 2015). While the impact of dense environments like clusters on galaxy evolution has been extensively studied (e.g. Dressler 1980; Poggianti et al. 2010; Marasco et al. 2023), the role of filaments remains less clear, particularly with respect to their ability to either enhance or suppress SF and AGN activity (e.g. Porter et al. 2008; Kraljic et al. 2018; Liao & Gao 2019; Malavasi et al. 2022). Due to this conflicting result, an effort to tackle this issue by using astronomical tools, in particular radio source count, has been a pivotal focus of this project.

In order to construct the source count, this work has used several well-established surveys and catalogues at multiple wavelengths to reside radio galaxies in filaments, where the surveys and catalogues include the RACS surveys (Hale et al. 2021; Duchesne et al. 2023), WISE × SCOS (Bilicki et al. 2016) and SDSS (Carrón Duque et al. 2022). These surveys and catalogues were then cross-matched to generate two distinct RAWS samples, classified according to the observing frequencies of the RACS surveys – 887.5 and 1367.5 MHz – resulting in the RAWS-low and RAWS-mid samples, respectively. The cross-matching procedure in this work has used a threshold resolution of about 6 arcsec to match with the angular resolution of the RACS surveys. The RAWS-low and RAWS-mid samples have been divided into several subsamples, which include all RAWS galaxies, RAWS filament galaxies and RAWS non-filament galaxies, where the last two subsamples are distinguishable based on the radio galaxies' position of whether or not these galaxies reside in filaments or fields. The number of galaxies for each subsample is given in Table 1.

Since it is well-established that AGNs dominate the 1.4-GHz Euclidean-normalized differential radio source counts, $S^{5/2}\,\mathrm{d}N/\mathrm{d}S$, above 1 mJy, (e.g. Becker et al. 1995; Condon et al. 1998; Padovani et al. 2015; D'Amato et al. 2022) as given in Table 3, it has been found that the majority of radio galaxies in our samples are dominated by AGN, instead of SFGs, which resulted from the sensitivity depths of the RACS-low and RACS-mid surveys. These radio source counts, presented in Fig. 3, reveal that the full RAWS-low and RAWS-mid samples, and their respective subsamples RAWS-low and RAWS-mid non-filament galaxy population show excellent agreement with previous deep radio surveys such as FIRST (Becker et al. 1995), ATESP (Prandoni et al. 2001), VLA-COSMOS (Bondi et al. 2008), the Lockman Hole Project (Prandoni et al. 2018), and MIGHTEE-COSMOS (Hale et al. 2022). This consistency across flux densities from approximately 3–100 mJy demonstrates the reliability of the samples and subsamples considered in this work.

However, the RAWS filament galaxy subsample for both RAWS-low and RAWS-mid shows a systematic deficit in source counts at flux densities below ∼3 mJy – precisely where SFGs and low-luminosity AGN are expected to dominate the radio population (e.g. Condon 1989; Mauch & Sadler 2007) – with the most significant suppression occurring from approximately 3 mJy and beyond for both samples. The observed discrepancy implies that the surface density of radio-emitting AGN is significantly lower within the filamentary large-scale structure of the cosmic web when compared to their counterparts residing in non-filamentary or field environments. Furthermore, this underdensity is also evident when contrasted with the radio source populations detected in blind surveys, which do not specifically target or isolate large-scale cosmic structures. This picture is further supported by the results of the KS test, which provides statistical evidence that the radio galaxy populations residing in filamentary structures are significantly influenced by the physical conditions and environmental characteristics of the filaments in which they are embedded.

This deficit supports the growing body of evidence that filaments may act as quenching environments for galaxies. Optical studies have shown declining sSFRs for galaxies with decreasing distance to filament spines (Alpaslan et al. 2016; Kuutma et al. 2017), accompanied by colour transformation and increasing early-type fractions (Kraljic et al. 2018; Castignani et al. 2022). Similarly, recent hydrodynamical simulations such as IllustrisTNG and Horizon-AGN

also report suppressed SFRs for galaxies residing near filaments, likely due to environmental pre-processing mechanisms such as gradual gas starvation (Dubois et al. 2014; Malavasi et al. 2022; Hasan et al. 2023). The downturn in source counts observed in this study, particularly for filament galaxies from approximately 3 mJy and above, is consistent with these results and suggests that filaments may regulate star-forming and AGN activity by limiting cold gas availability, either through strangulation, weak ram pressure, or cosmic web stripping by the intergalactic medium (IGM).

Conversely, several studies have proposed that filaments may play a role in enhancing SF under specific conditions, particularly in galaxies undergoing early stages of infall or gravitational interaction within the filamentary structure (Coppin et al. 2012; Darvish et al. 2014; Kotecha et al. 2022; Zheng et al. 2022). These scenarios often involve increased gas accretion or compression due to mild interactions, which could trigger short-lived bursts of SF before eventual quenching sets in. However, the source count analysis presented in this work reveals no such enhancement within the filament population. Instead, the differential source counts for filament galaxies consistently lie below those of the total RAWS samples and the non-filament subsamples, particularly in the low-flux regime that is typically dominated by normal SFGs (Garrett et al. 2000; Mauch et al. 2020). The absence of a star-forming excess, coupled with the suppression observed even above the RACS completeness threshold, indicates that environmental quenching mechanisms, such as ram-pressure stripping, strangulation, or reduced cold gas replenishment, are likely at play. These findings again support the hypothesis that, within the redshift range up to $z \sim 0.6$ and the galaxy populations probed by the RACS-low and RACS-mid surveys, the dominant environmental influence exerted by filaments is suppressive rather than stimulative with respect to galaxy activity.

To further develop the RAWS project, future works should focus specifically on a more detailed and comprehensive investigation of filament galaxies. By systematically characterizing the radio properties of galaxies embedded within filamentary structures, along with the incorporated properties observed in other wavelengths, it would be possible to gain deeper insight into the role of filaments in regulating AGN activity. Such analyses, which include constructing the radio luminosity functions, spectral index analysis and AGN evolutionary pathways across redshifts, would help clarify whether the environmental effects observed in clusters – particularly the suppression or enhancement of radio activity – are also prevalent in the lower density, dynamically distinct environments of filaments. This approach, which will be presented in the upcoming papers of this series, would contribute significantly to understanding how galaxy evolution is shaped by the diverse conditions across the cosmic web, particularly within the intermediate-density regime that filaments offer.

ACKNOWLEDGEMENTS

The authors acknowledge Universiti Malaya for their funding support under the Universiti Malaya Deputy Vice Chancellor's Grant with project number RUIP002-2023. This scientific work uses data obtained from Inyarrimanha Ilgari Bundara/the Murchison Radio-astronomy Observatory. We acknowledge the Wajarri Yamaji People as the traditional owners and native title holders of the observatory site. CSIRO's ASKAP radio telescope is part of the Australia Telescope National Facility (https://ror.org/05qajvd42). Operation of ASKAP was funded by the Australian Government with support from the National Collaborative Research Infrastructure Strategy. ASKAP uses the resources of the Pawsey Supercomputing Research Centre. Establishment of ASKAP, Inyarrimanha Ilgari Bundara, the CSIRO Murchison Radio-astronomy Observatory and the Pawsey Supercomputing Research Centre are initiatives of the Australian Government, with support from the Government of Western Australia and the Science and Industry Endowment Fund. This paper includes archived data obtained through the CSIRO ASKAP Science Data Archive, CASDA (https://data.csiro.au). This publication makes use of data products from the WISE, which is a joint project of the University of California, Los Angeles, and the Jet Propulsion Laboratory/California Institute of Technology, and NEOWISE, which is a project of the Jet Propulsion Laboratory/California Institute of Technology. WISE and NEOWISE were funded by the National Aeronautics and Space Administration. This research has also made use of data obtained from the SuperCOSMOS Science Archive, prepared and hosted by the Wide Field Astronomy Unit, Institute for Astronomy, University of Edinburgh, which was funded by the UK Science and Technology Facilities Council. For the reconstruction of cosmic filaments, this work has used the Cosmic Filament Catalogue from a paper entitled A Novel Cosmic Filament Catalogue from SDSS Data by Carrón Duque et al. (2022).

DATA AVAILABILITY

The radio data used in this study are retrieved from the Rapid ASKAP Continuum Survey (RACS-low and RACS-mid), which are publicly available via the CSIRO ASKAP Science Data Archive (CASDA) at https://casda.csiro.au. Optical and IR photometry and photometric redshift data are obtained from the WISE × SCOS catalogue, which combines ALLWISE and SuperCOSMOS data and is publicly accessible via the VizieR service or at http://ssa.roe.ac.uk/WISExSCOS. The cosmic filament catalogue used in this work is provided by Carrón Duque et al. (2022), and can be accessed publicly at https://www.javiercarron.com/catalogue, which contains filament reconstructions based on SDSS DR12 data.

REFERENCES

Abell G. O., 1958, ApJS, 3, 211
Alam S. et al., 2015, ApJS, 219, 12
Alpaslan M. et al., 2015, MNRAS, 451, 3249
Alpaslan M. et al., 2016, MNRAS, 457, 2287
Anderson L. et al., 2014, MNRAS, 441, 24
Bahcall N. A., 1988, ARA&A, 26, 631
Becker R. H., White R. L., Helfand D. J., 1995, ApJ, 450, 559
Bilicki M. et al., 2016, ApJS, 225, 5
Blanton M. R. et al., 2017, ApJ, 154, 28
Bondi M., Ciliegi P., Schinnerer E., Smolčić V., Jahnke K., Carilli C., Zamorani G., 2008, ApJ, 681, 1129
Bonjean V., Aghanim N., Douspis M., Malavasi N., Tanimura H., 2020, A&A, 638, A75
Bonzini M., Padovani P., Mainieri V., Kellermann K. I., Miller N., Rosati P., Tozzi P., Vattakunnel S., 2013, MNRAS, 436, 3759
Botteon A. et al., 2020, MNRAS, 499, L11
Carilli C. L., Taylor G. B., 2002, ARA&A, 40, 319
Carlberg R. G. et al., 1997, ApJ, 485, L13
Carrón Duque J., Migliaccio M., Marinucci D., Vittorio N., 2022, A&A, 659, A166
Castignani G. et al., 2022, ApJS, 259, 43
Cautun M., van de Weygaert R., Jones B. J. T., Frenk C. S., 2014, MNRAS, 441, 2923
Chen Y.-C. et al., 2017, MNRAS, 466, 1880
Chon G., Böhringer H., Zaroubi S., 2015, A&A, 575, L14
Coccato L. et al., 2019, MNRAS, 492, 2955
Cole S. et al., 2005, MNRAS, 362, 505

Collister A. A., Lahav O., 2004, PASP, 116, 345
Condon J. J., 1989, ApJ, 338, 13
Condon J. J., 1992, ARA&A, 30, 575
Condon J. J., Cotton W. D., Greisen E. W., Yin Q. F., Perley R. A., Taylor G. B., Broderick J. J., 1998, AJ, 115, 1693
Coppin K. E. K. et al., 2012, ApJ, 749, L43
D'Amato Q. et al., 2022, A&A, 668, A133
Darvish B., Sobral D., Mobasher B., Scoville N. Z., Best P., Sales L. V., Smail I., 2014, ApJ, 796, 51
Dawson K. S. et al., 2012, AJ, 145, 10
Donnan C. T., Tojeiro R., Kraljic K., 2022, Nat. Astron., 6, 599
Dressler A., 1980, ApJ, 236, 351
Driver S. P. et al., 2011, MNRAS, 413, 971
Dubois Y. et al., 2014, MNRAS, 444, 1453
Duchesne S. W. et al., 2023, Publ. Astron. Soc. Aust., 41 e003
Galárraga-Espinosa D., Aghanim N., Langer M., Gouin C., Malavasi N., 2020, A&A, 641, A173
Garrett M. A., de Bruyn A. G., Giroletti M., Baan W. A., Schilizzi R. T., 2000, A&A, 361, L41
Gehrels N., 1986, ApJ, 303, 336
Govoni F., Feretti L., 2004, Int. J. Mod. Phys. D, 13, 1549
Govoni F. et al., 2019, Science, 364, 981
Gray M. E., Taylor A. N., Meisenheimer K., Dye S., Wolf C., Thommes E., 2002, ApJ, 568, 141
Hale C. L. et al., 2021, Publ. Astron. Soc. Aust., 38, e058
Hale C. L. et al., 2022, MNRAS, 520, 2668
Hasan F. et al., 2023, ApJ, 950, 114
Helfand D. J., White R. L., Becker R. H., 2015, ApJ, 801, 26
Henkel B., Partridge R. B., 2005, ApJ, 635, 950
Herrera Ruiz N. et al., 2018, A&A, 616, A128
Huchra J. P. et al., 2012, ApJS, 199, 26
Jones C., Forman W., 1990, Adv. Space Res., 10, 209
Jones D. H. et al., 2004, MNRAS, 355, 747
Kinyumu M. K., Kimani N., Nyenge R., Obonyo W., 2023, MNRAS, 527, 1368
Kodama T., Smail I., Nakata F., Okamura S., Bower R. G., 2001, ApJ, 562, L9
Kotecha S. et al., 2022, MNRAS, 512, 926
Kraljic K. et al., 2018, MNRAS, 474, 547
Kravtsov A. V., Borgani S., 2012, ARA&A, 50, 353
Kuutma T., Tamm A., Tempel E., 2017, A&A, 600, L6
Laigle C. et al., 2018, MNRAS, 474, 5437
de Lapparent V., Geller M. J., Huchra J. P., 1986, ApJ, 302, L1
Liao S., Gao L., 2019, MNRAS, 485, 464
Liske J. et al., 2015, MNRAS, 452, 2087
Malavasi N., Langer M., Aghanim N., Galárraga-Espinosa D., Gouin C., 2022, A&A, 658, A113
Marasco A., Poggianti B. M., Fritz J., Werle A., Vulcani B., Moretti A., Gullieuszik M., Kulier A., 2023, MNRAS, 525, 5359
Matthews A. M., Condon J. J., Cotton W. D., Mauch T., 2021, ApJ, 909, 193
Mauch T., Sadler E. M., 2007, MNRAS, 375, 931
Mauch T. et al., 2020, ApJ, 888, 61
McConnell D. et al., 2020, Publ. Astron. Soc. Aust., 37, e048
Mohan N., Rafferty D., 2015, Astrophysics Source Code Library, record ascl:1502.007
Mohr J. J., Mathiesen B., Evrard A. E., 1999, ApJ, 517, 627
Montes M., Trujillo I., 2018, MNRAS, 482, 2838
O'Kane C. J., Kuchner U., Gray M. E., Aragón-Salamanca A., 2024, MNRAS, 534, 1682
Osinga E. et al., 2022, A&A, 665, A71
Padovani P., Bonzini M., Kellermann K. I., Miller N., Mainieri V., Tozzi P., 2015, MNRAS, 452, 1263
Peacock J. A., Hambly N. C., Bilicki M., MacGillivray H. T., Miller L., Read M. A., Tritton S. B., 2016, MNRAS, 462, 2085
Pimbblet K. A., Drinkwater M. J., Hawkrigg M. C., 2004, MNRAS, 354, L61
Poggianti B. M., De Lucia G., Varela J., Aragon-Salamanca A., Finn R., Desai V., von der Linden A., White S. D. M., 2010, MNRAS, 405, 995
Porter S. C., Raychaudhury S., Pimbblet K. A., Drinkwater M. J., 2008, MNRAS, 388, 1152
Postman M., Geller M. J., Huchra J. P., 1988, ApJ, 95, 267
Prandoni I., Gregorini L., Parma P., de Ruiter H. R., Vettolani G., Wieringa M. H., Ekers R. D., 2001, A&A, 365, 392
Prandoni I., Guglielmino G., Morganti R., Vaccari M., Maini A., Röttgering H. J. A., Jarvis M. J., Garrett M. A., 2018, MNRAS, 481, 4548
Pranger F. et al., 2013, A&A, 557, A62
Quintana H., Melnick J., Proust D., Infante L., 1997, A&AS, 125, 247
Scodeggio M. et al., 2018, A&A, 609, A84
Sousbie T., 2011, MNRAS, 414, 350
Stoica R. S., Martínez V. J., Mateu J., Saar E., 2005, A&A, 434, 423
Tully R. B., Courtois H., Hoffman Y., Pomarède D., 2014, Nature, 513, 71
Vollmer B., 2013, The Influence of Environment on Galaxy Evolution. Springer Netherlands, Dordrecht, p. 207
Vulcani B. et al., 2019, MNRAS, 487, 2278
White R. L., Becker R. H., Helfand D. J., Gregg M. D., 1997, ApJ, 475, 479
Wieringa M., Raja W., Ord S., 2020, in Pizzo R., Deul E. R., Mol J. D., de Plaa J., Verkouter H., eds, ASP Conf. Ser. Vol. 527, Astronomical Data Analysis Software and Systems XXIX. Astron. Soc. Pac., San Francisco, p. 591
Winkel N., Pasquali A., Kraljic K., Smith R., Gallazzi A., Jackson T. M., 2021, MNRAS, 505, 4920
Wright E. L. et al., 2010, AJ, 140, 1868
Xu W. et al., 2020, MNRAS, 498, 1839
York D. G. et al., 2000, AJ, 120, 1579
Zhang X. et al., 2024a, EAS2024, European Astronomical Society Annual Meeting. Cambridge University Press, p. 1474
Zhang C. et al., 2024b, MNRAS, 530, 4234
Zheng H., Liao S., Hu J., Gao L., Grand R. J. J., Gu Q., Guo Q., 2022, MNRAS, 514, 2488
Zwicky F., 1937, ApJ, 86, 217

SUPPORTING INFORMATION

Supplementary data are available at *MNRAS* online.

Table 3 (a).mrt
Table 3 (b).mrt

Please note: Oxford University Press is not responsible for the content or functionality of any supporting materials supplied by the authors. Any queries (other than missing material) should be directed to the corresponding author for the article.

This paper has been typeset from a TEX/LATEX file prepared by the author.